

Joint Geometric–Chemical Distance for Protein Surfaces

Himanshu Swami,^{1,*} John M. McBride,^{1,†} Jean-Pierre Eckmann,^{2,‡} and Tsvi Tlusty^{1,§}

¹*Department of Physics, Ulsan National Institute of Science and Technology, Ulsan 44919, South Korea*

²*Département de Physique Théorique et Section de Mathématiques, Université de Genève, Geneva, Switzerland*

Protein function is executed at the molecular surface, where shape and chemistry act together to govern interaction. Yet most comparison methods treat these aspects separately, privileging either global fold or local descriptors and missing their coupled organization. Here we introduce IFACE (Intrinsic Field–Aligned Coupled Embedding), a correspondence-based framework that aligns protein surfaces through probabilistic coupling of intrinsic geometry with spatially distributed chemical fields. From this alignment, we derive a joint geometric–chemical distance that integrates structural and physicochemical discrepancies within a single formulation. Across diverse proteins, this distance separates conformational variability from true structural divergence more effectively than fold-based similarity measures. Applied to the cytochrome P450 family, it reveals coherent family-level organization and identifies conserved buried catalytic pockets despite the complex topology. By linking interpretable surface correspondences with a unified distance, IFACE establishes a principled basis for comparing protein interfaces and detecting functionally related interaction patches across proteins.

INTRODUCTION

Proteins are macromolecular machines whose functions are realized through interaction^{1–7}. Recent advances in sequence-based structure prediction have largely resolved the determination of folded structure^{8–12}. What remains unresolved is how proteins should be compared as *inter-faces*^{13,14}. In molecular recognition, catalysis, and regulation, functional specificity is encoded at the surface rather than in the folded core¹⁵.

A protein surface consists of solvent-exposed side chains forming a curved interface¹⁶ where geometry and chemistry act together. Local curvature constrains approach; electrostatic potential mediates long-range interaction; hydrophobic patterning and hydrogen-bonding propensity regulate short-range specificity^{17–20}. Various surface constructions are used in practice, such as the van der Waals surface, the solvent-accessible surface (SAS), and the solvent-excluded surface (SES). The van der Waals surface is defined as the union of atomic spheres with their van der Waals radii²¹. The solvent-accessible surface (SAS) is obtained by tracing the center of a spherical probe representing a solvent molecule as it rolls over the van der Waals surface²². The related solvent-excluded surface (SES) corresponds to the boundary of the volume that the probe cannot enter, and therefore approximates the surface physically encountered by the solvent or a binding partner²³. We focus on the solvent-excluded surface, though the framework extends to alternative definitions.

Despite their functional importance, there is no clear physical framework for comparing protein surfaces. Existing approaches typically evaluate properties such as geometry, electrostatics, or chemical composition separately, even though these features are physically coupled. Deep-learning methods infer surface similarity from data^{24–28}, but similarity is encoded implicitly in trained representations and depends on task-specific supervision. In most cases, both training and evaluation rely on downstream objectives—such as binding-site or interface prediction—so similarity is defined indirectly through task performance rather than through an explicit comparison framework. The resulting scores can predict functional outcomes, but surface similarity is encoded implicitly in learned representations rather than defined by an explicit geometric–chemical

comparison. Classical geometric schemes^{29–34} analyze intrinsic surface geometry but do not account for chemical properties. In both cases, geometry and chemistry are either treated independently or combined only through task-dependent training.

In contrast, we derive an explicit symmetric distance that jointly encodes geometric and chemical information within a unified variational framework. The construction produces interpretable correspondences between surfaces rather than task-specific similarity scores and does not rely on downstream supervision or prediction objectives.

Conceptually, a protein surface may be viewed as a curved manifold endowed with intrinsic geometric distances and spatially organized chemical feature fields. A meaningful notion of similarity must therefore *relate fields across geometry*. This requires a correspondence between surfaces that maps points on one surface to points on the other, enabling chemical features to be compared while simultaneously accounting for intrinsic surface geometry. Without such a mapping, geometric distortion and physicochemical mismatch cannot be integrated into a single comparison.

We therefore construct a symmetric geometric–chemical distance from a variational correspondence between surfaces. Each surface is represented by its intrinsic geometry together with spatially distributed chemical fields defined on the surface. Pairs of surfaces are related through a soft probabilistic map obtained by variational optimization. This map establishes a common reference between the two surfaces, allowing geometric and chemical discrepancies to be combined within a single metric. The resulting distance is intrinsic, symmetric, and directly interpretable through the induced surface correspondence.

We demonstrate the framework in two representative settings. First, we test discrimination between distinct conformers of the same protein and genuinely different proteins. We define a structural distance derived from intrinsic geometry and a chemical distance based on hydrogen-bonding propensity, hydrophobicity, and electrostatic potential. Their combination yields the IFACE distance, integrating both contributions within one formulation. IFACE separates conformational variability from inter-protein dissimilarity more effectively than the traditional TM-distance, defined as $1 - \text{TM-score}$ ³⁵.

Second, we examine similarity at the family level. In this regime, each protein pair occupies a point in a distance space defined by joint surface organization rather than fold alone. Applied to the cytochrome P450 family^{36,37}, the framework produces natural clustering that reflects shared surface organization beyond global geometry. The IFACE distance thus captures functionally relevant aspects of protein interfaces and provides a principled basis for applications such as ligand substitution and structure-guided drug discovery.

The IFACE Method. We introduce IFACE (Intrinsic Field–Aligned Coupled Embedding), a correspondence-based framework for comparing protein surfaces through coupled geometry and chemical fields. Figure 1 summarizes the construction. Given two protein surfaces, S_α and S_β , each surface is represented by its intrinsic geometric structure together with spatially distributed physico-chemical feature fields, including electrostatics, hydrogen-bond propensity, hydrophobicity, and curvature (Fig. 1a). We then compute an optimal coupling matrix that aligns the two surfaces by balancing structural consistency with feature-field agreement (Fig. 1b). The relative contribution of these terms is controlled by the parameter λ , introduced explicitly in the variational formulation below.

The resulting coupling defines soft correspondences between surface points and induces bidirectional surface maps between the two proteins (Fig. 1c). Using these correspondences, we compute symmetric structural and feature-field discrepancies (Fig. 1d). From these quantities, we construct dataset-normalized structural and chemical distances and define the IFACE distance as their joint geometric—chemical combination.

This procedure yields a symmetric distance that integrates intrinsic geometry with transported chemical fields while preserving interpretable surface mappings. Full details of the optimization and distance definitions are provided in the Methods section.

Our implementation depends on a few parameter choices, as seen in Fig. 1b, in particular λ and ϵ . They measure the relative weights of the geometric and chemical aspects of the problem, as well as the relative weight given to the errors. We have checked that, in reasonable domains of these parameters, the results are qualitatively stable and quantitatively similar (see details in SI).

RESULTS

The proposed method is evaluated on a diverse set of protein surfaces. Unless stated otherwise, all surfaces are represented by meshes with 3,000 vertices; details of surface generation are provided in the Supplementary Information. The framework is purely distance-based and does not involve deep learning, supervised training, or data-driven model fitting. All comparisons arise directly from the variational correspondence between surfaces.

We begin with a basic but essential consistency test. If the representation faithfully encodes surface organization, distinct conformers of the same protein should remain close to one another, while remaining clearly separated from unrelated proteins, when embedded in the structural–chemical

feature space defined by the IFACE metric. We therefore compare IFACE distances among conformers of the same protein with distances between different proteins. This experiment probes whether conformational variability is correctly distinguished from genuine inter-protein dissimilarity.

We then consider a more demanding regime: clustering at the protein-family level across species. Here, we test whether proteins belonging to the same family, but originating from different organisms, group together under the IFACE metric. This setting probes whether shared functional surface organization outweighs species-specific structural variation. Successful clustering indicates that the representation captures conserved geometric–chemical patterns rather than superficial sequence similarity or organismal origin. Such behavior is directly relevant to protein search, ligand substitution, and structure-guided drug discovery.

IFACE discerns conformers of the same protein as closer than different proteins.

In this task, we use the ATLAS dataset³⁸ and focus on four proteins with PDB codes³⁹ 6XR_X⁴⁰, 5HZ7⁴¹, 2XZ3⁴², and 6XDS⁴³, corresponding to an AEG12 mosquito protein, a DNA-binding protein, a viral protein, and a signaling protein, respectively. Importantly, these structures are artificial constructs in which the proteins of interest are fused to maltose-binding protein (MBP), a commonly used solubility and crystallization tag. Consequently, each structure contains the same MBP domain in addition to the native protein. All structures were restricted to chain A. ATLAS contains Molecular Dynamics (MD) trajectories for 1,390 proteins from the Protein Data Bank (PDB), with three independent simulations per protein and 10,001 snapshots per trajectory. Each trajectory spans 100 ns. On this timescale, the native fold is preserved; what fluctuates is the surface. The resulting ensembles, therefore, sample thermal surface variability without crossing into large conformational rearrangements. This makes ATLAS suitable for assessing whether a distance captures intrinsic surface fluctuations rather than gross structural change.

To construct a stringent benchmark, we searched for proteins that allow controlled comparison both within and between proteins. Sequence analysis using MMseqs2⁴⁴ showed that most ATLAS entries are mutually unrelated, aside from occasional duplicates. A notable exception is a set of four related synthetic constructs fused to maltose-binding protein for crystallization: 6XR_X_A⁴⁰, 5HZ7_A⁴¹, 2XZ3_A⁴², and 6XDS_A⁴³. These proteins are similar enough to make discrimination nontrivial, yet distinct enough to test whether surface chemistry and geometry add resolving power beyond fold similarity.

For each protein, we select ten conformers sampled along the MD trajectory. Conformers are chosen such that the resulting TM-score distributions overlap both within proteins and across proteins. Consequently, the corresponding TM-distance (defined as $1 - \text{TM-score}$) provides only partial separation, as illustrated by the normalized TM distances in Fig. 3a. This creates an ensemble in which intra-protein variability competes directly with inter-protein similarity. This resulting overlap makes the

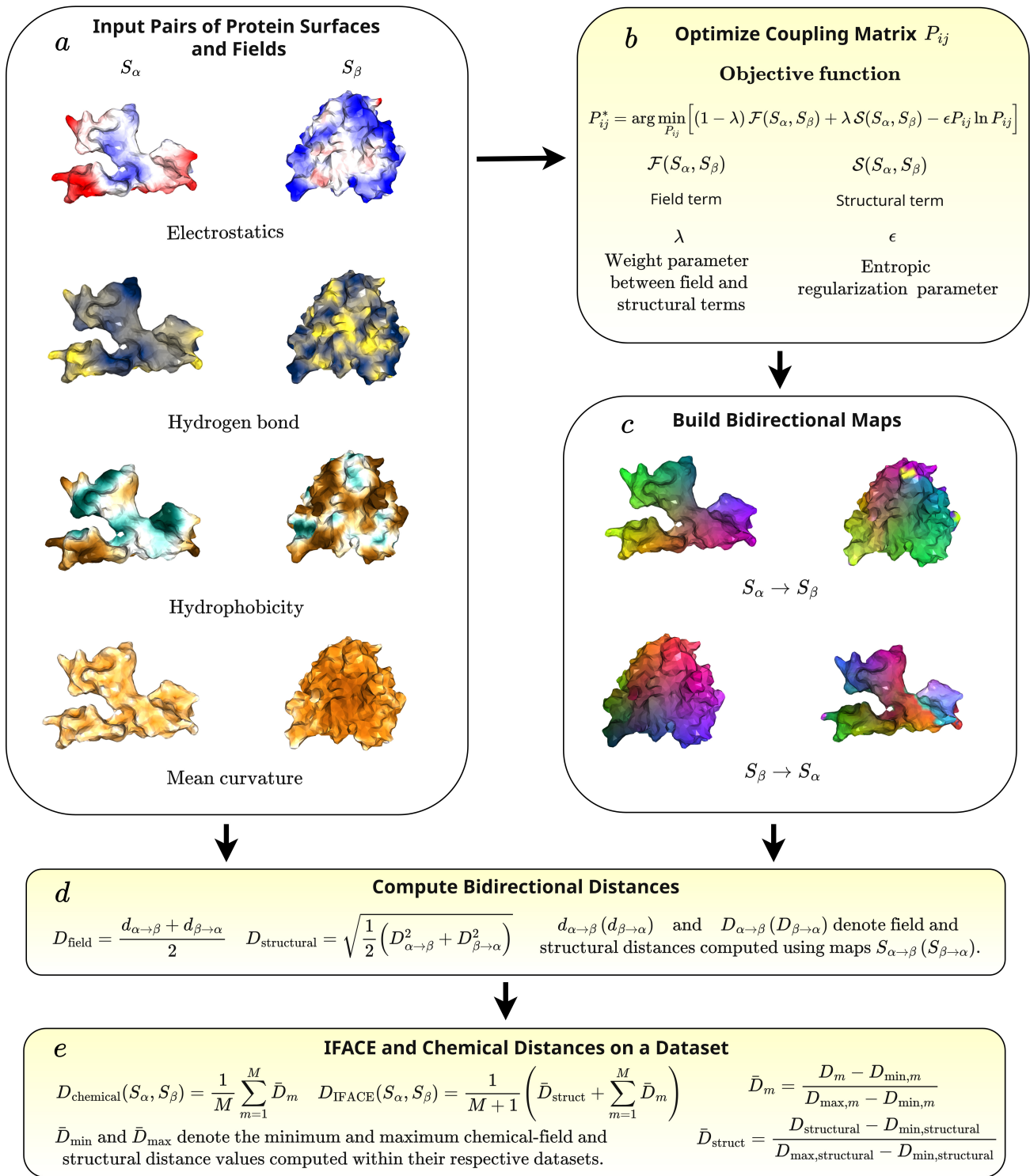


FIG. 1. **Conceptual workflow of IFACE.** (a) Protein surfaces S_α and S_β are represented using geometry and surface feature fields (electrostatics, hydrogen-bond propensity, hydrophobicity, and curvature). (b) An optimal coupling matrix P_{ij} is computed by balancing structural and feature-field similarity. (c) The coupling defines bidirectional soft correspondences between surfaces. (d) Correspondence-based structural and feature-field distances are computed. (e) Distances are normalized across the dataset; their combination defines the IFACE and chemical distances derived from the structural distance and M feature-field distances.

dataset demanding. It asks whether a surface-based optimal coupling, sensitive to both geometry and physicochemical fields, can resolve what fold-level similarity cannot.

Example of IFACE mapping. Before turning to quantitative analysis, we first examine a representative example to visu-

alize the surface correspondences identified by the IFACE optimal transport coupling (Fig. 2). The mapping integrates geometric alignment with multiple physicochemical feature field –hydrophobicity, hydrogen-bond propensity, electrostatic potential, and mean curvature – as described above.

The two proteins shown (6XRX and 6XDS) have a TM-

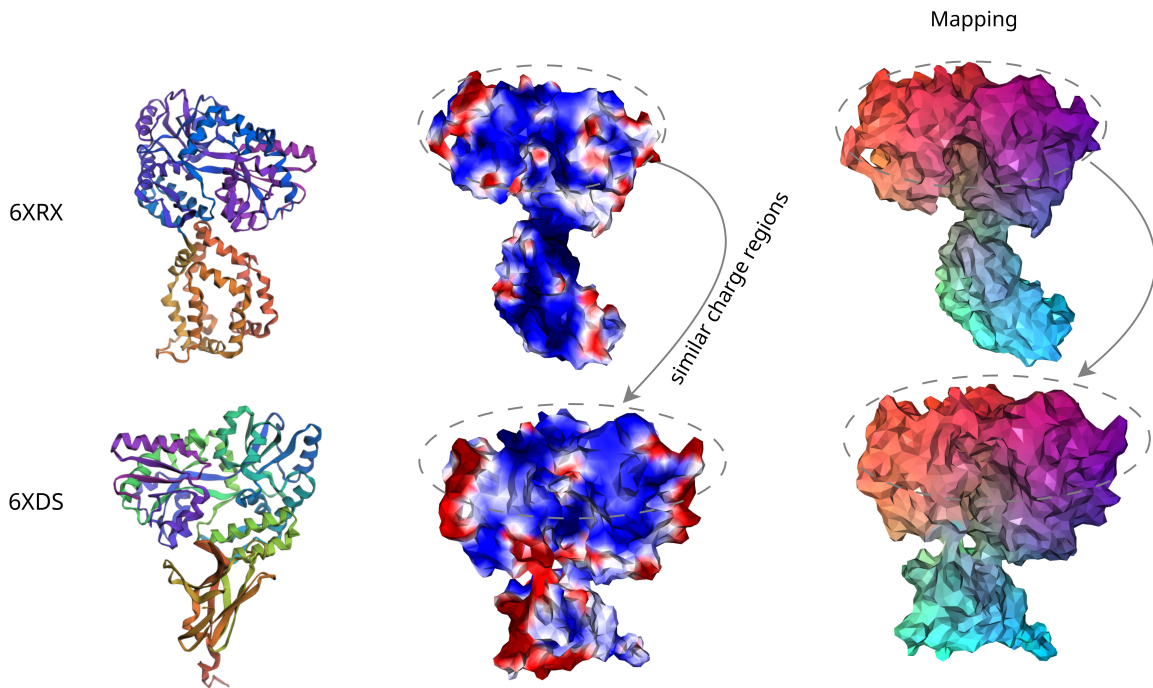


FIG. 2. **Comparison and mapping of protein surfaces.** Protein 6XRX is shown in the top row and 6XDS in the bottom row. Left: ribbon representations of the protein structures. Middle: electrostatic potential distributions (color scale clipped to the 5th–95th percentile of the combined distribution), where similar colors indicate regions with comparable electrostatic potential. Right: IFACE color mappings showing correspondences from 6XRX to 6XDS. The correspondences (vertex mapping) are computed using combined structural and feature-field similarity, allowing direct comparison of corresponding surface regions.

distance of ~ 0.30 (TM-score ~ 0.70), indicating substantial global fold similarity. This similarity arises because both constructs contain the same fused maltose-binding protein (MBP) domain, which is identical in sequence in the two structures. As a result, a large portion of the structures is effectively the same, leading to strong global alignment. The native proteins themselves have distinct biological functions, so any meaningful structural differences are expected to occur outside the MBP fusion region, primarily at the surface or within the non-MBP domains.

The top row of Fig. 2 displays the electrostatic potential mapped onto the two surfaces. The upper regions of 6XRX (lipid-binding protein) and 6XDS (signaling protein) exhibit closely matched electrostatic profiles and compatible geometry. The IFACE correspondence (rightmost panel) aligns these regions across the two proteins, identifying surface patches that are jointly similar in shape and physicochemical character. In contrast, the lower regions differ in both curvature and electrostatics, and consequently contribute more strongly to the overall distance.

This example illustrates how the optimal transport coupling integrates geometric and chemical information to resolve surface-level similarity beyond fold alignment alone. Having established this qualitative intuition, we now proceed to a systematic evaluation of whether the method reliably groups distinct conformers of the same protein.

IFACE distance robustly separates conformations from distinct proteins. We quantify discriminatory power using the *IFACE distance*, a composite measure that integrates structural and physicochemical features of pro-

TABLE I. Distances statistics and classification performance between conformers of the same protein and distinct proteins. Values are mean \pm s.d.; classification performance is reported as AP, average precision; AUC, area under the ROC curve.

Distance	Intra-protein	Inter-protein	AUC	AP
TM	0.17 ± 0.11	0.28 ± 0.024	0.82	0.74
Structural	0.21 ± 0.17	0.54 ± 0.16	0.92	0.89
Chemical	0.28 ± 0.17	0.65 ± 0.079	0.99	0.98
IFACE	0.27 ± 0.16	0.62 ± 0.069	0.99	0.97

tein surfaces. Each component—structural (*struct*), hydrophobicity (*hphob*), hydrogen-bond propensity (*hbond*), and electrostatic potential (*elect*)—is first normalized to the unit interval $[0, 1]$ to ensure comparable scale.

The IFACE distance is then defined as

$$\text{iface} = \frac{1}{4}(\text{struct} + \text{hphob} + \text{hbond} + \text{elect}),$$

assigning equal weight to geometric structure and to each chemical field. This equal-weight choice avoids parameter tuning and provides a transparent baseline against which more elaborate weighting schemes could be assessed. For comparison, we also define a *chemical-feature distance*,

$$\text{chemical} = \frac{1}{3}(\text{hphob} + \text{hbond} + \text{elect}),$$

which isolates the contribution of physicochemical fields independent of structural alignment.

Figure 3 compares TM-distance with the structural, chemical, and IFACE surface-based distances across four protein families (6XRX lipid binding, 5HZ7 DNA binding,

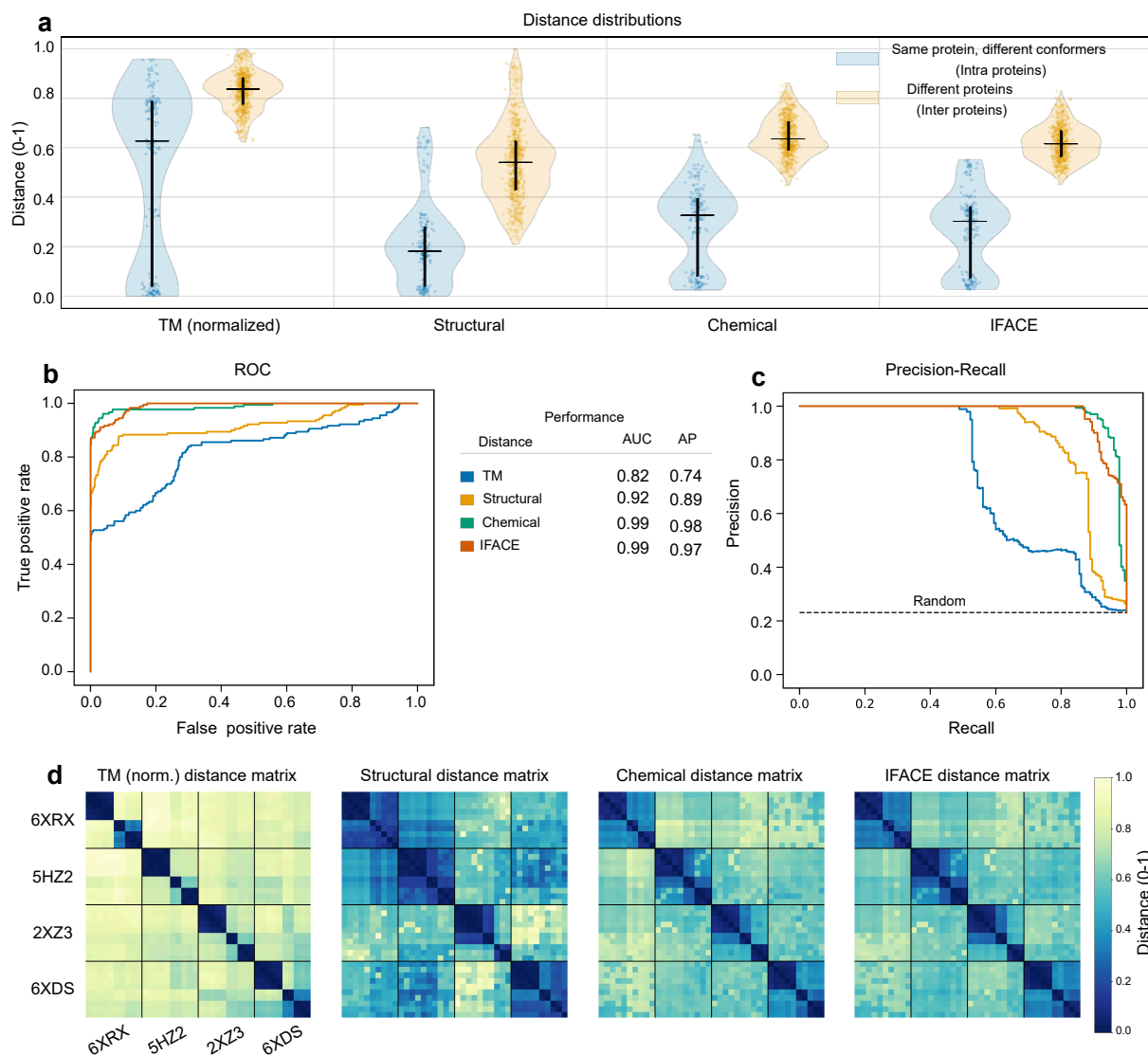


FIG. 3. Comparison of TM-distance and surface-based distances for separating conformers of the same protein from distinct proteins. (a) Distance distributions for TM (normalized [0, 1]), structural, chemical, and IFACE distances, comparing intra-protein conformers and inter-protein comparisons across four proteins (6XRX, 5HZ7, 2XZ3, and 6XDS). (b) Receiver operating characteristic (ROC) curves showing classification performance of each distance metric. (c) Precision-recall curves with the random baseline indicated by a dashed line. (d) Distance matrices grouped by protein. Surface-based distances produce clearer block-diagonal structure than TM-distance, indicating stronger intra-protein similarity and inter-protein separation.

2XZ3 viral, and 6XDS signaling). TM-distance exhibits substantial overlap between intra-protein conformers and inter-protein comparisons (Fig. 3a), indicating limited resolution in this regime. A quantitative summary of distance statistics and classification performance is provided in Table I.

In contrast, surface-based distances yield markedly improved separation. Structural surface distance reduces overlap, while chemical and IFACE distances achieve near-complete separation of conformers from distinct proteins. Notably, the chemical distance is more stable across conformational fluctuations than the purely structural measure, indicating that surface chemistry varies less under thermal motion than geometric detail.

Although the optimal weighting of components is not known *a priori*, the equal-weight IFACE distance already outperforms TM-distance decisively (AUC \sim 0.98, AP \sim 0.95). Receiver-operating and precision-recall curves (Fig. 3b,c) confirm robust discrimination between conformers of the same protein and unrelated proteins.

Distance matrices (Fig. 3d) further clarify the structure of the embeddings. TM-distance exhibits weak family-level organization. In contrast, surface-based distances produce clear block-diagonal structure, reflecting stronger intra-family similarity and enhanced inter-family separation.

Family-level similarity of proteins. We next test whether

TABLE II. List of PDB IDs and their source organisms

PDB ID	Source organism
2IJ5	Mycobacterium tuberculosis (bacterium)
6N6Q	Mycobacterium phage Adler (virus)
3OFU	Novosphingobium aromaticivorans (bacterium)
6ZI2	Streptomyces antibioticus (bacterium)
6UX0	Acanthamoeba castellanii str. Neff (amoeba)
4H23	Priestia megaterium (bacterium)
1JPZ	Priestia megaterium (bacterium)
1TQN	Homo sapiens (mammal)
2DN1	Homo sapiens (mammal)
1AOI	Xenopus laevis (amphibian; histone protein)
5Y0C	Homo sapiens (mammal; histone protein)
3L40	Schizosaccharomyces pombe (fungus)

the proposed distances organize proteins coherently at the family level. Using structural, feature-field, and combined IFACE distances, each protein pair is embedded in a space defined by joint surface organization. This construction yields a distance-based representation of protein space and allows direct comparison across families without reliance on sequence or fold annotations.

We focus on the cytochrome P450 family and compare intra-family relationships with distances to structurally unrelated proteins. The evaluation dataset consists of 12 protein structures drawn from diverse organisms, including bacteria, virus, amoeba, human, amphibian, and fungus (Table II). This cross-organism composition ensures that family-level similarity must emerge despite evolutionary divergence.

The P450 protein set comprises the following PDB entries: 2IJ5, 6N6Q, 3OFU, 6ZI2, 6UX0, 4H23, 1JPZ, and 1TQN. Each contains the characteristic heme (HEM) pocket that defines the catalytic center of the P450 family. As an external reference, we include hemoglobin (PDB ID 2DN1), which also binds heme but belongs to a distinct structural and functional class. In addition, three structurally unrelated proteins are incorporated for comparison: histones 1AOI and 5Y0C, and 3L40, a protein involved in genome stability and cell-cycle maintenance.

This curated, cross-organism dataset provides a controlled benchmark for assessing whether surface-based distances distinguish P450 proteins from non-P450 proteins, and whether family-level surface organization persists across evolutionary diversity.

Example of pocket mapping within the same protein family. We illustrate surface correspondence within the P450 family using full-length human cytochrome P450 3A4 (PDB ID: 1TQN, sequence length 486, chain A) and P450 BM-3 from *Bacillus megaterium* (PDB ID: 1JPZ, sequence length 473, chain A). Both proteins contain a heme prosthetic group coordinated by a conserved cysteine residue. The heme pocket is deeply buried, with substrate access occurring through channels or tunnels. Its internal topology—comprising cavities, handles, and narrow passages—renders it difficult to identify using surface-comparison schemes such as conformational mapping or projection onto a plane or sphere.

Figure 4 compares proteins 1JPZ and 1TQN. The top

TABLE III. Distance statistics and classification performance for P450-family discrimination. Values are mean \pm s.d. AP, average precision; AUC, area under the ROC curve.

Distance	Intra-family	Inter-protein	AUC	AP
Structural	0.28 ± 0.12	0.81 ± 0.11	1.00	1.00
Chemical	0.36 ± 0.12	0.62 ± 0.17	0.90	0.89
IFACE	0.34 ± 0.10	0.67 ± 0.15	0.99	0.99

row shows ribbon representations of 1JPZ (left) and 1TQN (right), with the heme prosthetic group highlighted in red. The bottom-left image highlights in red the surface patch surrounding the heme in 1JPZ, which mediates substrate oxidation via oxygen activation. This patch lies within the protein interior and is accessed through substrate tunnels, exemplifying nontrivial internal surface geometry. The bottom-right image shows the corresponding mapped region in 1TQN (blue), identifying the homologous buried pocket.

The probabilistic surface correspondence recovers this conserved internal organization despite substantial geometric complexity. The alignment identifies functionally equivalent regions without requiring global topological simplification, indicating that the joint geometric–chemical distance captures intrinsic surface structure rather than superficial shape similarity.

Surface-distance based clustering of protein surfaces. We next test whether surface distances organize proteins at the family level. We compare homologs within the P450 family both with one another and with proteins from other families. In Fig. 5, we frame this as a classification task: distinguish P450–P450 pairs from P450–non-P450 pairs using three metrics — structural, chemical, and IFACE distances.

Fig. 5a shows the distributions of pairwise distances. For all three metrics, intra-family comparisons concentrate at shorter distances, whereas inter-family comparisons shift to larger values. The separation is quantified in Table III.

The observed distance separation translates directly into classification performance (Fig. 5b,c). Structural distance achieves perfect discrimination (AUC = 1.00, AP = 1.00). IFACE distance is nearly perfect (AUC = 0.99, AP = 0.99). Chemical distance alone remains strongly discriminative (AUC = 0.90, AP = 0.89), well above the random baseline (AP = 0.47). Because the structurally coherent dataset is relatively small, the perfect structural classification likely reflects the limited scope of this benchmark rather than general structural separability across broader protein space. The distance matrices (Fig. 5d) display a block-diagonal pattern, with P450 proteins forming a compact intra-family cluster and larger distances to non-P450 proteins across all surface-based metrics.

We next assess whether this separation extends to higher-level organization. Thus, we ask whether families emerge as coherent clusters in the full distance space. To this end, we performed hierarchical clustering using structural, hydrogen-bond propensity, hydrophobicity, electrostatic, chemical, and IFACE distances, and compared the resulting dendrograms and clustering-quality metrics (Fig. 6).

Structural and IFACE distances produce the clear-

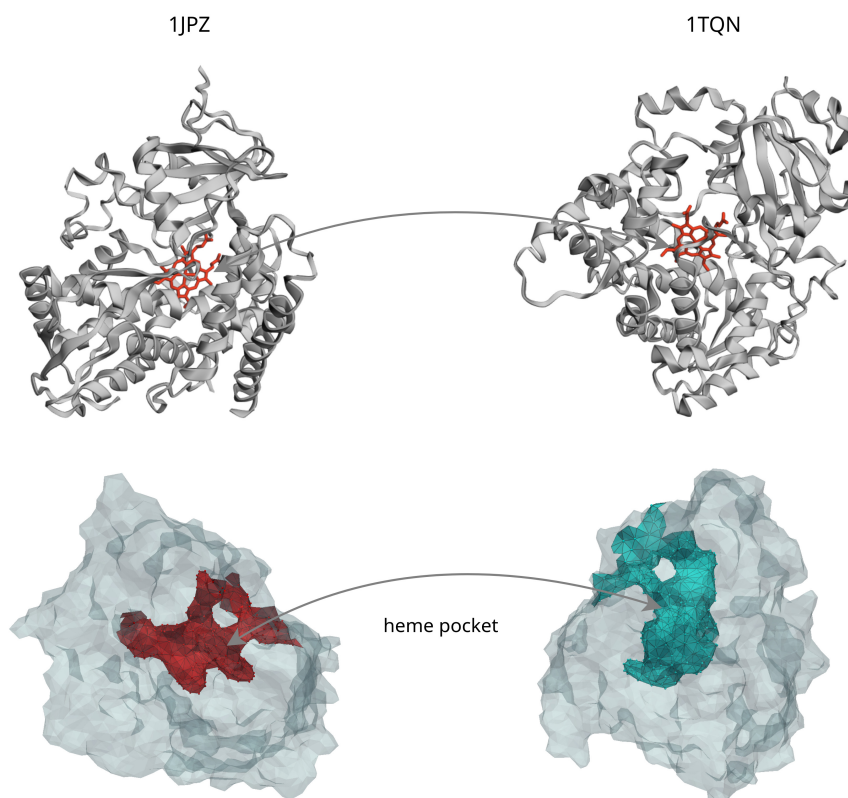


FIG. 4. **Comparison of proteins 1JPZ and 1TQN.** Top row: ribbon representations of chain A from 1JPZ (left) and 1TQN (right), with the heme prosthetic group shown in red. Bottom left: patch around the heme on 1JPZ (red), containing the heme group responsible for substrate oxidation via oxygen activation. This patch lies within the protein interior and is accessed through substrate tunnels, illustrating non-trivial internal surface geometry. Bottom right: corresponding mapped region on 1TQN (blue), demonstrating that the method identifies a similar buried pocket across proteins.

est family-level organization (Fig. 6a,f): P450 proteins cluster compactly, while histone, hemoglobin, and cell-maintenance proteins separate consistently. Hydrogen-bond and hydrophobicity distances recover this structure with weaker separation. Electrostatic distance yields the least stable organization (Fig. 6b–d). Chemical distance, which integrates multiple physicochemical features, generates clustering comparable to the structural distance (Fig. 6e).

Clustering-quality metrics quantify these observations (Fig. 6g). Cophenetic correlation measures how faithfully the dendrogram preserves pairwise distances; ARI and purity measure agreement with known family assignments. With these measures, we find that the structural, hydrogen-bond, and IFACE distances achieve high cophenetic correlations (0.94, 0.93, and 0.95, respectively) and perfect agreement with the annotated family labels (ARI = 1.00, purity = 1.00). In contrast, the hydrophobic, electrostatic, and chemical distances show weaker agreement.

Taken together, these results show that combining geometry with physicochemical surface fields, as in IFACE, yields a stable and discriminative family-level organization within this benchmark.

DISCUSSION

We introduced a correspondence-based framework for comparing protein surfaces through coupled geometry and chemical fields. By constructing an optimal surface correspondence, the method yields both a quantitative geometric–chemical distance and explicit, interpretable surface mappings. Surface similarity is thus defined through transport between manifolds rather than through separate structural and chemical descriptors.

In the analysis of four proteins presented here, surface-based distances distinguished conformational variability from genuine protein divergence more effectively than fold-based similarity measures. Incorporating coupled surface organization reduced overlap between intra-protein conformers and inter-protein comparisons, indicating that functional information resides in surface geometry and physicochemical patterning beyond global fold alignment.

At the family level, the framework organized cytochrome P450 proteins coherently across species. Structural distances captured shared geometric organization, chemical distances captured complementary physicochemical similarity, and their combination in the IFACE distance produced stable separation between P450 and non-P450 proteins. These results indicate that functional relationships are encoded in coupled surface organization rather than in fold similarity alone.

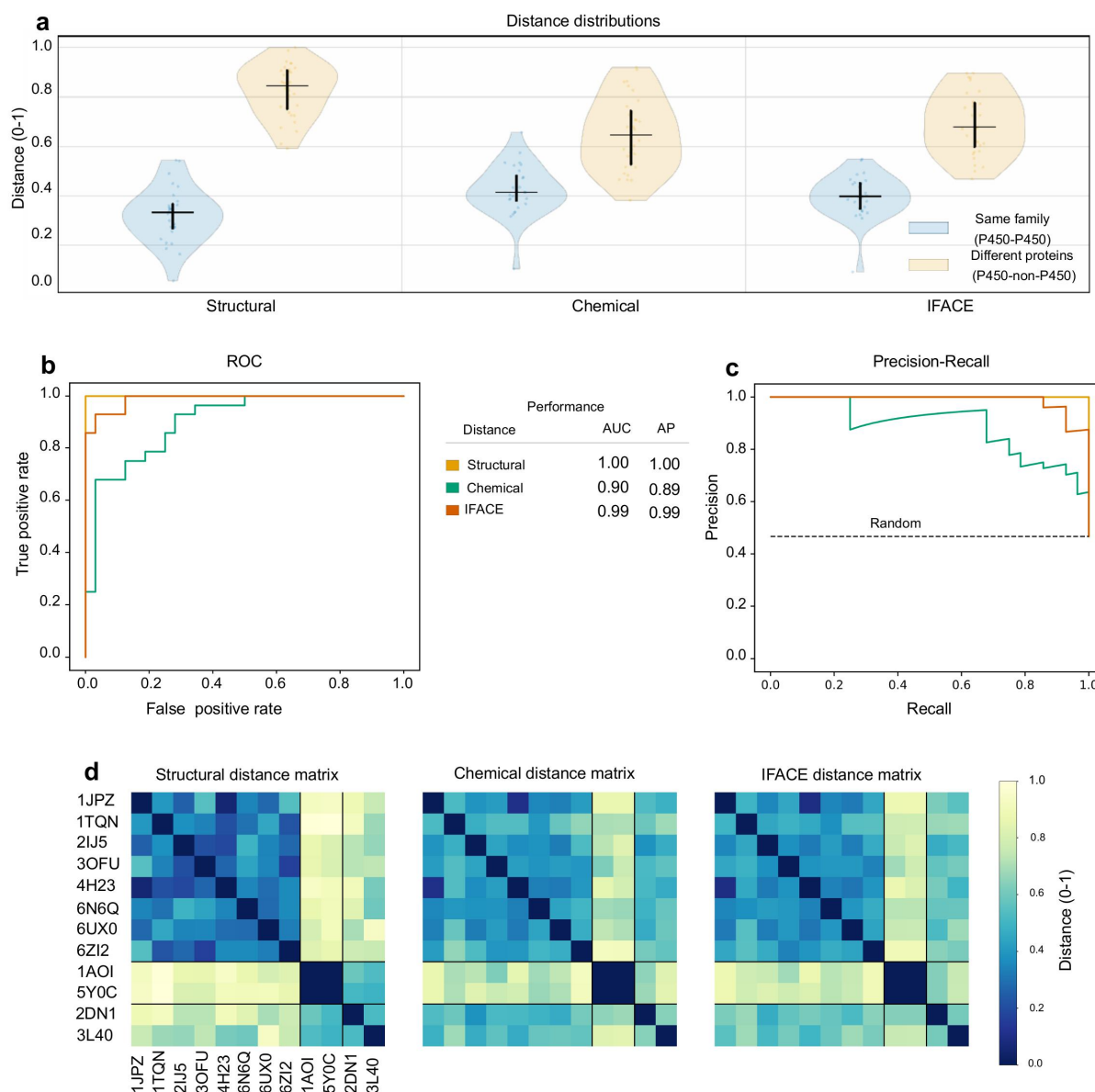


FIG. 5. Surface-distance-based characterization of protein pairs involving cytochrome P450s. (a) Distance distributions for structural, chemical, and IFACE distances, comparing same-family (P450–P450) and different-family (P450–non-P450) protein pairs. (b) Receiver operating characteristic (ROC) curves showing family-level classification performance. (c) Precision–recall curves with the random baseline indicated by a dashed line. (d) Distance matrices for structural, chemical, and IFACE distances. P450 proteins form a coherent block separated from histone, hemoglobin, and cell-maintenance proteins, demonstrating consistent family-level separation.

More generally, the framework defines protein–surface similarity as a geometric–chemical comparison mediated by explicit correspondence. Because the mapping is interpretable, the method supports both global classification and local analysis of conserved surface patches. This dual capability enables systematic comparison of functional interfaces without reliance on task-specific supervision.

Several limitations warrant consideration. The present implementation relies on a finite set of scalar surface fields and a balance parameter regulating geometric and chemical contributions. Although performance is robust within the datasets examined here, broader validation across more diverse protein families will further test generality. Extensions to additional feature types, including vector or tensor

fields, and to alternative surface representations may refine the correspondence and distance definitions.

Despite these limitations, the central contribution is structural rather than empirical: protein–surface similarity can be formulated as a coupled geometric–chemical comparison mediated by transport between surfaces. This formulation provides a physically explicit basis for analyzing biological interfaces and establishes a principled foundation for comparing functional protein surfaces.

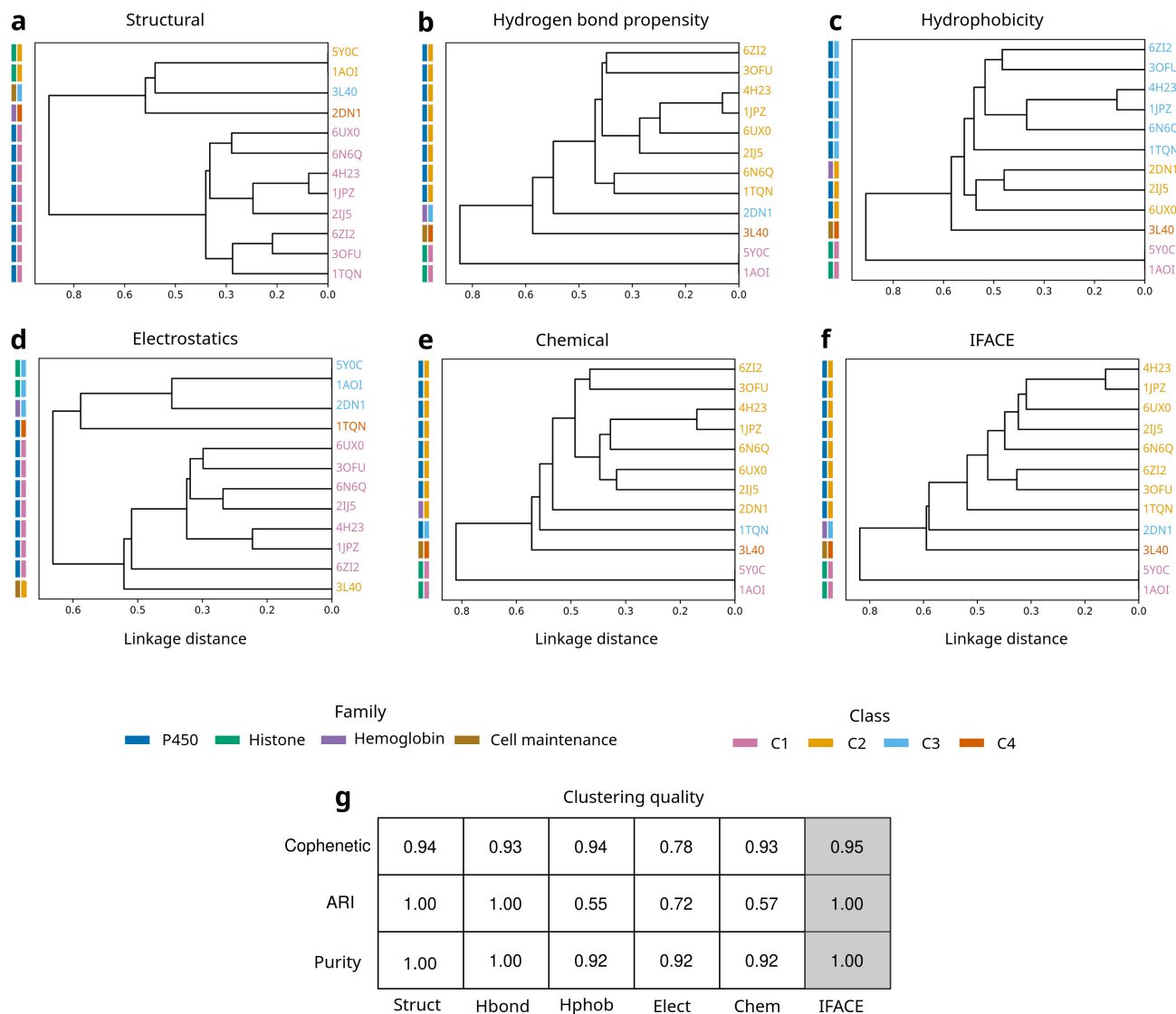


FIG. 6. Hierarchical clustering of proteins using structural and physicochemical surface distances. (a–f) Dendrograms computed using structural, hydrogen-bond propensity, hydrophobicity, electrostatic, chemical, and IFACE distances, respectively. Colored bars indicate protein family (P450, histone, hemoglobin, and cell-maintenance) and cluster assignment. (g) Clustering-quality metrics comparing distance types, including cophenetic correlation, adjusted Rand index (ARI), and purity. Structural and IFACE distances show the most consistent recovery of family-level organization.

METHODS

In this section, we describe how distances between protein surfaces are constructed within the IFACE framework. The key step is the identification of a soft correspondence between two surfaces, encoded in an optimal coupling matrix that relates their surface vertices.

A working implementation of the IFACE framework, including surface preprocessing, coupling computation, and distance evaluation, is available on GitHub: github.com/ihswami/iface

Optimal Coupling Matrix. We consider two protein surfaces, S_α and S_β , represented as triangulated meshes and endowed with m physicochemical feature fields, denoted f_m^α and f_m^β . Our central objective is to relate these two surfaces in a manner that respects *both* their geometric structure and their surface chemistry. To achieve this, we introduce a probabilistic, or *soft*, correspondence between the

surfaces, encoded by a *coupling matrix* \mathbf{P} . Each matrix element P_{ij} quantifies the degree to which vertex i on S_α corresponds to vertex j on S_β . By avoiding a rigid one-to-one assignment, this formulation permits a flexible comparison of surface regions and naturally accommodates structural variability and chemical heterogeneity.

The coupling matrix is constrained by prescribed marginal distributions over the vertices of each surface, ρ^α and ρ^β , such that $\sum_j P_{ij} = \rho_i^\alpha$ and $\sum_i P_{ij} = \rho_j^\beta$. These marginals assign weights to surface elements based on local surface area, while simultaneously encoding the spatial organization and characteristic scale of the chemical feature fields. In this sense, they serve as composite landmarks: locally anchoring the correspondence while remaining sensitive to the global geometry of the surface. The explicit construction of these distributions is described in the Supplementary Information.

The optimal coupling matrix \mathbf{P} is determined by balanc-

ing two complementary contributions. The first is a *field term*, which compares the physicochemical feature fields defined on the two surfaces. The second is a *structural term*, which enforces geometric compatibility between surface shapes. The optimal correspondence emerges from reconciling these two contributions under the marginal constraints above, yielding a coupling that reflects both chemical similarity and geometric coherence. We now define these two terms explicitly.

Field Term. The field term \mathcal{F} quantifies the mismatch between feature fields on the two surfaces. For optimization purposes, it is defined as

$$\mathcal{F}(S_\alpha, S_\beta) = \sum_{i,j,m} P_{ij} \left[\frac{f_{m,i}^\alpha - f_{m,j}^\beta}{\sigma^m} \right]^2, \quad (1)$$

where σ^m denotes the standard deviation of the m^{th} feature field, computed using values from both surfaces. This normalization places all fields on a comparable scale and promotes the matching of vertices with similar physicochemical signatures.

Structural Term. The structural term enforces consistency between the intrinsic geometries of the two surfaces. To this end, we construct for each surface S its geodesic distance matrix D_{ij}^S on the unit-normalized mesh, supplemented by a smoothing kernel H_{ij}^S that incorporates global geometric information. These are combined as $G_{ij}^S = D_{ij}^S + \epsilon_g H_{ij}^S$, with $S \in \{S_\alpha, S_\beta\}$. Here, the smoothing kernel is $H_{ij}^S = \sum_k K_{ik}^S K_{kj}^S$, with $K_{ip}^S = \exp[-(D_{ip}^S)^2 / (2\sigma_S^2)]$. Thus, H^S encodes smoothed, long-range geometric correlations derived from the geodesic metric. Using these definitions, the structural discrepancy between surfaces S_α and S_β is given by

$$\mathcal{S}(S_\alpha, S_\beta) = \sum_{i,j,k,l} P_{ik} P_{jl} \left(G_{ij}^\alpha - G_{kl}^\beta \right)^2. \quad (2)$$

In our analysis, σ_S is chosen as a fixed fraction of the maximum geodesic distance, $\sigma_S = 0.1 D_{\max}^S$, and the weight ϵ_g is set to 0.1 to ensure that the global contribution remains a perturbative correction of the geodesic structure. In the limit $\epsilon_g = 0$, this term reduces to the classical Gromov–Wasserstein objective, with $G_{ij}^S \rightarrow D_{ij}^S$ ^{45,46}.

Optimization. To determine the coupling matrix, we minimize the following entropic-regularized objective function:

$$P_{ij}^* = \arg \min_{P_{ij}} \left[(1 - \lambda) \mathcal{F}(S_\alpha, S_\beta) + \lambda \mathcal{S}(S_\alpha, S_\beta) - \epsilon \sum_{i,j} P_{ij} \log P_{ij} \right], \quad (3)$$

where the minimization is subject to the constraints $\sum_j P_{ij} = \rho_i^\alpha$ and $\sum_i P_{ij} = \rho_j^\beta$. The entropic term $-\epsilon \sum_{i,j} P_{ij} \log P_{ij}$ plays a distinct and complementary role to the geometric regularization controlled by ϵ_g . While ϵ_g smooths the *metric structure* entering the structural term, the entropy promotes diffuseness of the coupling itself, suppressing spurious sharp correspondences and stabilizing the optimization landscape. In practice, this regularization improves convergence and prevents the solution from becoming trapped in shallow local minima.

To find the optimal coupling, we proceed in several stages. We first obtain an initial alignment of the meshes using a combination of rigid and feature-field-aware non-rigid alignment, based on mean curvature, hydrophobicity, hydrogen bonding, and electrostatic potential. This alignment is converted into an initial coupling matrix using a Gaussian kernel followed by Sinkhorn normalization^{47,48} to enforce the marginal constraints. The resulting coupling serves as a warm start for minimizing the entropic-regularized objective. Finally, for refinement, the entropic regularization is gradually reduced and ultimately turned off, yielding a sharper coupling matrix P_{ij}^* . Full algorithmic details are provided in the Supplementary Information. We next describe how distances between protein surfaces are constructed from the resulting coupling matrix.

IFACE Distance. We construct distances between protein surfaces by leveraging the optimal coupling to compare both chemical feature fields and geometric structure. The guiding principle is to use only the most reliable portions of the correspondence: for each vertex, we retain the two most confidently mapped vertices on the opposing surface. Feature values are transported across the coupling, evaluated at the mapped vertices, and compared using the l^1 norm, *i.e.*, absolute value. The choice of the l^1 norm is deliberate: it suppresses the influence of outliers that can arise from discretization effects, where feature values may vary unevenly across meshes of differing resolution, thereby yielding a more robust estimate of chemical dissimilarity.

To ensure symmetry, all comparisons are performed *bidirectionally*. In addition, prior to computing distances, feature fields are mildly regularized by local smoothing. For each vertex i , the field value is updated using its neighborhood according to

$$f_i \equiv f_i + \epsilon_f \sum_k \exp(-D_{ik}/\beta_i) f_k,$$

where D is the geodesic distance matrix and β_i is chosen as the characteristic distance of the 2-ring neighborhood of vertex i . Throughout this work, we fix $\epsilon_f = 0.1$.

Using these smoothed fields, the feature-field distance D_{field} is defined as

$$d_{\alpha \rightarrow \beta} = \sum_{i,q} \omega_i^q \|f_i^\alpha - f_{y_i^q}^\beta\|_{l^1}, \quad d_{\beta \rightarrow \alpha} = \sum_{j,r} \eta_j^r \|f_j^\beta - f_{x_j^r}^\alpha\|_{l^1},$$

$$D_{\text{field}}(S_\alpha, S_\beta) = \frac{d_{\alpha \rightarrow \beta} + d_{\beta \rightarrow \alpha}}{2}, \quad (4)$$

where ω_i^q and η_j^r are confidence weights associated with the vertex mappings $i \rightarrow y_i^q \in \{y^j\}$ and $j \rightarrow x_j^r \in \{x^i\}$, respectively. These weights are normalized such that $\sum_{q=1}^2 \omega_i^q = 1$ and $\sum_{r=1}^2 \eta_j^r = 1$, ensuring that only the relative confidence between the two dominant correspondences enters the distance.

The structural distance is constructed analogously using a bidirectional comparison of the structural matrices G^α and G^β , which are computed from the original protein meshes rather than the unit-normalized meshes. It is de-

defined as

$$D_{\text{structure}}(S_\alpha, S_\beta) = \frac{1}{\sqrt{2}} \left(\sum_{i,j,q,p} \omega_i^q \omega_j^p \|G_{ij}^\alpha - G_{y_j y_i^p}^\beta\|^2 + \sum_{k,l,r,s} \eta_k^r \eta_l^s \|G_{x_k x_l^s}^\alpha - G_{kl}^\beta\|^2 \right)^{\frac{1}{2}}. \quad (5)$$

All notation follows the definitions introduced above. This construction yields a symmetric structural distance that reflects discrepancies in intrinsic geometry while remaining tightly coupled to the most confident regions of the surface correspondence.

To combine the structural and feature-field distances into a unified surface-comparison distance, we next define dataset-normalized chemical and IFACE distances. The chemical distance is defined by aggregating discrepancies across all chemical surface fields. For each chemical field i , we use the bidirectional field distance $D_m(S_\alpha, S_\beta)$ defined above and normalize it across the dataset using min-max normalization,

$$\bar{D}_m = \frac{D_m - D_{\min,m}}{D_{\max,m} - D_{\min,m}}, \quad (6)$$

where $D_{\min,m}$ and $D_{\max,m}$ denote the minimum and maximum non-trivial observed values of D_m within the dataset. This normalization scales each feature-field distance to the interval $[0, 1]$, improving interpretability and enabling consistent comparison across different fields. The trivial case of identical surfaces (distance = 0) is excluded when defining $D_{\min,m}$.

The overall chemical distance is defined as the average of the normalized chemical feature-field distances,

$$D_{\text{chemical}}(S_\alpha, S_\beta) = \frac{1}{M} \sum_{m=1}^M \bar{D}_m, \quad (7)$$

where M denotes the number of chemical feature fields. The structural distance is normalized across the dataset in the same way,

$$\bar{D}_{\text{struct}} = \frac{D_{\text{struct}} - D_{\min,\text{struct}}}{D_{\max,\text{struct}} - D_{\min,\text{struct}}}. \quad (8)$$

Finally, the IFACE distance is defined as the average of the normalized structural distance and the normalized chemical feature-field distances,

$$D_{\text{IFACE}}(S_\alpha, S_\beta) = \frac{1}{M+1} \left(\bar{D}_{\text{struct}} + \sum_{m=1}^M \bar{D}_m \right). \quad (9)$$

Because the normalization depends on the evaluated dataset, we briefly clarify its implications. Each component is normalized independently and combined symmetrically; therefore, proteins that are close in both structural and feature-field spaces remain close under both the chemical and IFACE distances. Upon expansion of the dataset, updated values of D_{\min} and D_{\max} may modify the normalized components and consequently the absolute chemical and IFACE distance values. However, since the same rescaling is applied consistently within each feature, relative proximity relationship, and thus the overall clustering structure,

are preserved by IFACE and chemical distances. Significant deviations may occur only in cases where proximity is predominantly driven by a single component and dataset expansion substantially alters its normalization range.

* swamihimanshush@gmail.com

† jmmcbride@protonmail.com

‡ jean-pierre.eckmann@unige.ch

§ tsvitlusty@gmail.com

- [1] J. Janin and F. Rodier, Protein–protein interaction at crystal contacts, *Proteins: Structure, Function, and Bioinformatics* **23**, 580 (1995).
- [2] L. H. Hartwell, J. J. Hopfield, S. Leibler, and A. W. Murray, From molecular to modular cell biology, *Nature* **402**, C47 (1999).
- [3] D. S. Goodsell and A. J. Olson, Structural symmetry and protein function, *Annual review of biophysics and biomolecular structure* **29**, 105 (2000).
- [4] T. Tlusty, A. Libchaber, and J.-P. Eckmann, Physical model of the genotype-to-phenotype map of proteins, *Physical Review X* **7**, 021037 (2017).
- [5] S. Dutta, J.-P. Eckmann, A. Libchaber, and T. Tlusty, Green function of correlated genes in a minimal mechanical model of protein evolution, *Proceedings of the National Academy of Sciences* **115**, E4559 (2018).
- [6] T. Tlusty and A. Libchaber, Life sets off a cascade of machines, *Proceedings of the National Academy of Sciences* **122**, e2418000122 (2025).
- [7] E. Weinreb, J. M. McBride, M. Siek, J. Rougemont, R. Renault, Y. Peleg, T. Unger, S. Albeck, Y. Fridmann-Sirkis, S. Lushchekina, *et al.*, Enzymes as viscoelastic catalytic machines, *Nature Physics* **21**, 787 (2025).
- [8] C. B. Anfinsen, Principles that govern the folding of protein chains, *Science* **181**, 223 (1973).
- [9] C. Chothia and A. M. Lesk, The relation between the divergence of sequence and structure in proteins., *The EMBO journal* **5**, 823 (1986).
- [10] J. Jumper, R. Evans, A. Pritzel, T. Green, M. Figurnov, O. Ronneberger, K. Tunyasuvunakool, R. Bates, A. Židek, A. Potapenko, *et al.*, Highly accurate protein structure prediction with alphafold, *nature* **596**, 583 (2021).
- [11] M. Baek, F. DiMaio, I. Anishchenko, J. Dauparas, S. Ovchinnikov, G. R. Lee, J. Wang, Q. Cong, L. N. Kinch, R. D. Schaeffer, *et al.*, Accurate prediction of protein structures and interactions using a three-track neural network, *Science* **373**, 871 (2021).
- [12] J. M. McBride, K. Polev, A. Abdirasulov, V. Reinharz, B. A. Grzybowski, and T. Tlusty, AlphaFold2 can predict single-mutation effects, *Physical Review Letters* **131**, 218401 (2023).
- [13] M. C. Lawrence and P. M. Colman, Shape complementarity at protein/protein interfaces (1993).
- [14] A. Shulman-Peleg, R. Nussinov, and H. J. Wolfson, Recognition of functional sites in protein structures, *Journal of molecular biology* **339**, 607 (2004).
- [15] S. Jones and J. M. Thornton, Analysis of protein-protein interaction sites using surface patches, *Journal of molecular biology* **272**, 121 (1997).
- [16] F. M. Richards, Areas, volumes, packing, and protein structure, *Annual review of biophysics and bioengineering* **6**, 151 (1977).
- [17] F. B. Sheinerman, R. Norel, and B. Honig, Electrostatic aspects of protein–protein interactions, *Current opinion in structural biology* **10**, 153 (2000).
- [18] J. Kyte and R. F. Doolittle, A simple method for displaying the hydropathic character of a protein, *Journal of molecular biology* **157**, 105 (1982).
- [19] T. Kortemme, A. V. Morozov, and D. Baker, An orientation-dependent hydrogen bonding potential improves prediction of specificity and structure for proteins and protein–protein complexes, *Journal of molecular biology* **326**, 1239 (2003).
- [20] J. Konc and D. Janežič, Protein- protein binding-sites prediction by protein surface structure conservation, *Journal of chemical information and modeling* **47**, 940 (2007).
- [21] A. v. Bondi, van der waals volumes and radii, *The Journal of physical chemistry* **68**, 441 (1964).
- [22] B. Lee and F. M. Richards, The interpretation of protein structures: estimation of static accessibility, *Journal of molecular biology* **55**, 379 (1971).
- [23] M. L. Connolly, Analytical molecular surface calculation, *Applied Crystallography* **16**, 548 (1983).
- [24] P. Gainza, F. Sverrisson, F. Monti, E. Rodola, D. Boscaini, M. M. Bronstein, and B. E. Correia, Deciphering interaction fingerprints from protein molecular surfaces using geometric deep learning, *Nature methods* **17**, 184 (2020).
- [25] M. Simonovsky and J. Meyers, Deeplytough: learning structural comparison of protein binding sites, *Journal of chemical information and modeling* **60**, 2356 (2020).
- [26] S. K. Mylonas, A. Axenopoulos, and P. Daras, Deepsurf: a surface-based deep learning approach for the prediction of ligand binding sites on proteins, *Bioinformatics* **37**, 1681 (2021).
- [27] S. Riahi, J. H. Lee, T. Sorenson, S. Wei, S. Jager, R. Olfati-Saber, Y. Zhou, A. Park, M. Wendt, H. Minoux, *et al.*, Surface id: a geometry-aware system for protein molecular surface comparison, *Bioinformatics* **39**, btad196 (2023).
- [28] Y. Lin, L. Pan, Y. Li, Z. Liu, and X. Li, Exploiting hierarchical interactions for protein surface learning, *IEEE Journal of Biomedical and Health Informatics* **28**, 1927 (2024).
- [29] D. La, J. Esquivel-Rodríguez, V. Venkatraman, B. Li, L. Sael, S. Ueng, S. Ahrendt, and D. Kihara, 3d-surfer: software for high-throughput protein surface comparison and analysis, *Bioinformatics* **25**, 2843 (2009).
- [30] S. Yin, E. A. Proctor, A. A. Lugovskoy, and N. V. Dokholyan, Fast screening of protein surfaces using geometric invariant fingerprints, *Proceedings of the National Academy of Sciences* **106**, 16622 (2009).
- [31] V. Venkatraman, Y. D. Yang, L. Sael, and D. Kihara, Protein-protein docking using region-based 3d zernike descriptors, *BMC bioinformatics* **10**, 407 (2009).
- [32] D. Kihara, L. Sael, R. Chikhi, and J. Esquivel-Rodriguez, Molecular surface representation using 3d zernike descriptors for protein shape comparison and docking, *Current Protein and Peptide Science* **12**, 520 (2011).
- [33] J. Hass and P. Koehl, How round is a protein? exploring protein structures for globularity using conformal mapping, *Frontiers in molecular biosciences* **1**, 26 (2014).
- [34] X. Zhu, Y. Xiong, and D. Kihara, Large-scale binding ligand prediction by improved patch-based method patch-surfer2.0, *Bioinformatics* **31**, 707 (2015).
- [35] Y. Zhang and J. Skolnick, Tm-align: a protein structure alignment algorithm based on the tm-score, *Nucleic acids research* **33**, 2302 (2005).
- [36] F. P. Guengerich, Cytochrome p450 and chemical toxicology, *Chemical research in toxicology* **21**, 70 (2008).
- [37] T. Omura, Structural diversity of cytochrome p450 enzyme system, *Journal of biochemistry* **147**, 297 (2010).
- [38] Y. Vander Meersche, G. Cretin, A. Gheeraert, J.-C. Gelly, and T. Galochkina, Atlas: protein flexibility description from atomistic molecular dynamics simulations, *Nucleic acids research* **52**, D384 (2024).
- [39] H. M. Berman, J. Westbrook, Z. Feng, G. Gilliland, T. N. Bhat, H. Weissig, I. N. Shindyalov, and P. E. Bourne, The protein data bank, *Nucleic acids research* **28**, 235 (2000).
- [40] A. C. Y. Foo, P. M. Thompson, S.-H. Chen, R. Jadi, B. Lupo, E. F. DeRose, S. Arora, V. C. Placentra, L. Premkumar, L. Perera, L. C. Pedersen, N. Martin, and G. A. Mueller, The mosquito protein AEG12 displays both cytolytic and antiviral properties via a common lipid transfer mechanism, *Proc. Natl. Acad. Sci. U.S.A.* **118**, 10.1073/pnas.2019251118 (2021).
- [41] J.-L. Berry, Y. Xu, P. N. Ward, S. M. Lea, S. J. Matthews,

- and V. Pelicic, A Comparative Structure/Function Analysis of Two Type IV Pilin DNA Receptors Defines a Novel Mode of DNA Binding, *Structure* **24**, 926 (2016).
- [42] D. Lamb, A. W. Schüttelkopf, D. M. F. Van Aalten, and D. W. Brighty, Charge-Surrounded Pockets and Electrostatic Interactions with Small Ions Modulate the Activity of Retroviral Fusion Proteins, *PLoS Pathog* **7**, e1001268 (2011).
- [43] N. J. Byrne, A. C. Lee, J. Kostas, J. C. Reid, A. T. Partridge, S.-S. So, J. E. Cowan, P. Abeywickrema, H. Huang, M. Zebisch, J. J. Barker, S. M. Soisson, A. Brooun, and H.-P. Su, Development of a robust crystallization platform for immune receptor TREM2 using a crystallization chaperone strategy, *Protein Expression and Purification* **179**, 105796 (2021).
- [44] M. Steinegger and J. Söding, Mmseqs2 enables sensitive protein sequence searching for the analysis of massive data sets, *Nature biotechnology* **35**, 1026 (2017).
- [45] F. Mévoli, Gromov–wasserstein distances and the metric approach to object matching, *Foundations of computational mathematics* **11**, 417 (2011).
- [46] T. Vayer, L. Chapel, R. Flamary, R. Tavenard, and N. Courty, Fused gromov-wasserstein distance for structured objects: theoretical foundations and mathematical properties, arXiv preprint arXiv:1811.02834 (2018).
- [47] R. Sinkhorn, Diagonal equivalence to matrices with prescribed row and column sums, *The American Mathematical Monthly* **74**, 402 (1967).
- [48] M. Cuturi, Sinkhorn distances: Lightspeed computation of optimal transport, *Advances in neural information processing systems* **26** (2013).
- [49] M. A. Fischler and R. C. Bolles, Random sample consensus: a paradigm for model fitting with applications to image analysis and automated cartography, *Communications of the ACM* **24**, 381 (1981).
- [50] P. J. Besl and N. D. McKay, Method for registration of 3-d shapes, in *Sensor fusion IV: control paradigms and data structures*, Vol. 1611 (Spie, 1992) pp. 586–606.
- [51] Y. Chen and G. Medioni, Object modelling by registration of multiple range images, *Image and vision computing* **10**, 145 (1992).
- [52] A. Myronenko and X. Song, Point set registration: Coherent point drift, *IEEE transactions on pattern analysis and machine intelligence* **32**, 2262 (2010).
- [53] R. Flamary, N. Courty, A. Gramfort, M. Z. Alaya, A. Boissunon, S. Chambon, L. Chapel, A. Corenflos, K. Fstras, N. Fournier, L. Gautheron, N. T. Gayraud, H. Janati, A. Rakotomamonjy, I. Redko, A. Rolet, A. Schutz, V. Seguy, D. J. Sutherland, R. Tavenard, A. Tong, and T. Vayer, Pot: Python optimal transport, *Journal of Machine Learning Research* **22**, 1 (2021).
- [54] R. Flamary, C. Vincent-Cuaz, N. Courty, A. Gramfort, O. Kachaiev, H. Quang Tran, L. David, C. Bonet, N. Cassereau, T. Gnassounou, E. Tanguy, J. Delon, A. Collas, S. Mazelet, L. Chapel, T. Kerdoncuff, X. Yu, M. Feickert, P. Krzakala, T. Liu, and E. Fernandes Montesuma, *Pot python optimal transport (version 0.9.5)* (2024).

Supplementary Materials

THE GENERAL IFACE FRAMEWORK

Let S_α and S_β be two protein surfaces, each equipped with a collection of fields $F^\alpha = \{f_m^\alpha\}$ and $F^\beta = \{f_m^\beta\}$, where each $f_m^\alpha : S_\alpha \rightarrow \mathbb{R}^{n_m}$ and $f_m^\beta : S_\beta \rightarrow \mathbb{R}^{n_m}$ may represent a scalar field ($n_m = 1$), a vector field, or a tensor field. Although protein surfaces can be described more richly using vector and tensor fields (*e.g.*, electric fields, stress–strain, and polarizability tensors), they are still studied predominantly with scalar fields. Therefore, in this work, we restrict our analysis to **scalar** fields on protein surfaces—such as electrostatic potential, hydrogen bonding propensity, and hydrophobicity. Our goal is to define a distance metric $D(S_\alpha, S_\beta)$ that jointly captures both geometric and field-level differences.

From Diffeomorphic Mapping to Probabilistic Soft Mapping for Field Transport. Two surfaces are considered equivalent when there exists a diffeomorphism that maps one to the other while leaving all transported fields unchanged, *i.e.*,

$$S_\alpha \sim S_\beta \iff \exists \varphi \in \text{Diff}(S_\alpha, S_\beta) \text{ such that } \varphi^* F^\alpha = F^\beta, \quad (10)$$

Here, $\varphi^* F^\beta$ denotes the family of fields on S_α obtained by pulling back (φ^*) the fields in F^β via the diffeomorphism $\varphi : S_\alpha \rightarrow S_\beta$. Equivalently, the similarity between the pull-back fields and the native fields can be quantified using L^p norms. We define the pullback distance between families of scalar fields as the ℓ^1 -sum of the componentwise L^p distances:

$$d_F^{(p)}(F^\alpha, F^\beta; \varphi) := \sum_m \left(\int |f_m^\alpha - \varphi^* f_m^\beta|^p d\mu^\alpha \right)^{\frac{1}{p}}. \quad (11)$$

Here, $p \geq 1$ denotes the exponent of the L^p norm. $d\mu^\alpha$ denotes the surface-area measure on the surface (S_α) and it is given by $d\mu^\alpha \equiv \sqrt{|g_\alpha(x)|} d^2x$, where $|g_\alpha(x)|$ is the determinant of the metric tensor on the surface S_α . Further, to compare the internal geometric structure, we compare the metric tensor fields using the pushforward map φ_* :

$$d_G^{(q)}(g_\alpha, g_\beta; \varphi) := \left(\int_{S_\beta} \|\varphi_* g_\alpha - g_\beta\|^q d\mu^\beta \right)^{\frac{1}{q}}. \quad (12)$$

Here $d\mu^\beta$ denotes the surface area measure on S_β , $q \geq 1$ is the exponent for the geometric discrepancy, and $\|\cdot\|$ denotes a pointwise tensor norm. The exponents p and q control the sensitivity of the field and geometric discrepancies, respectively. Furthermore, similar expressions can be obtained for the inverse mapping φ^{-1} . We can now define a distance measure, $D(S_\alpha, S_\beta)$, using the diffeomorphism mapping, as follows

$$D(S_\alpha, S_\beta) = \sum_m \zeta_m \left(\frac{1}{2} \left(\int_{S_\alpha} |f_m^\alpha - \varphi^* f_m^\beta|^p d\mu^\alpha + \int_{S_\beta} |f_m^\beta - \varphi^{-1*} f_m^\alpha|^p d\mu^\beta \right) \right)^{\frac{1}{p}} + \eta \left(\frac{1}{2} \left(\int_{S_\beta} \|\varphi_* g_\alpha - g_\beta\|^q d\mu^\beta + \int_{S_\alpha} \|\varphi^{-1*} g_\beta - g_\alpha\|^q d\mu^\alpha \right) \right)^{\frac{1}{q}}. \quad (13)$$

Here ζ_m and η denote weighting coefficients for the m^{th} scalar field and the metric tensor discrepancy, respectively. These weights control the relative importance of the terms and provide normalization so that the resulting quantities are dimensionless or measured in the same units. We note that the above metric (Eq. 13) is clearly symmetric under the exchange, $S_\alpha \leftrightarrow S_\beta$, and furthermore, it can be shown that it satisfies the properties of a metric.

Probabilistic Soft Mapping. We have described a distance metric that assumes the existence of a diffeomorphism between the surfaces. However, protein surfaces are often corrupted by noise and limited resolution and an *exact* diffeomorphism rarely exists, even between two conformers of the *same* protein. Therefore, rather than searching for a single hard map $\varphi : S_\alpha \rightarrow S_\beta$, we relax the correspondence to a probability distribution on the product space $S_\alpha \times S_\beta$. In other words, we allow each point $x \in S_\alpha$ to match several points $y \in S_\beta$ with varying likelihoods. In addition, this approach has the advantage that, instead of producing a continuous map, it can probabilistically map different parts of proteins that have similar patches. For example, two proteins may share only a pocket, while the other parts of the proteins differ from each other.

Formally, we introduce a coupling $p(x, y)$.

$$p(x, y) \in \mathcal{P}(S_\alpha \times S_\beta), \quad p(x, y) \geq 0,$$

$$\int_{S_\alpha} p(x, y) d\mu^\alpha(x) = \rho^\beta(y), \quad \int_{S_\beta} p(x, y) d\mu^\beta(y) = \rho^\alpha(x), \quad (14)$$

where $\rho^\alpha(x)$ and $\rho^\beta(y)$ are the marginal distributions on the respective spaces. These marginal distributions represent, in a physical sense, the probability–or weight–with which each point on the surface should be considered when being mapped to the other. They can be chosen according to prior knowledge about which regions of one surface are more likely to be present and have a correspondence to regions on the other. They satisfy the normalization conditions:

$$\int_{S_\alpha} \rho^\alpha(x) d\mu^\alpha(x) = 1, \quad \int_{S_\beta} \rho^\beta(y) d\mu^\beta(y) = 1, \quad (15)$$

which ensure that ρ^α and ρ^β are valid probability density functions on S_α and S_β , respectively. Incorporating these into the Eq. 13 leads to a distance which we call the soft distance:

$$\begin{aligned}
D_{\text{soft}}(S_\alpha, S_\beta) = & \\
& \sum_m \zeta_m \left(\frac{1}{2} \int_{S_\alpha} \int_{S_\beta} |f_\alpha^m(x) - f_\beta^m(y)|^p p(x, y) d\mu^\alpha(x) d\mu^\beta(y) \right. \\
& \left. + (S_\alpha \leftrightarrow S_\beta) \right)^{\frac{1}{p}} + \eta \left(\frac{1}{2} \int_{S_\alpha} \int_{S_\beta} \|g_\alpha(x) - g_\beta(y)\|^q p(x, y) \right. \\
& \left. d\mu^\alpha(x) d\mu^\beta(y) + (S_\alpha \leftrightarrow S_\beta) \right)^{\frac{1}{q}}. \tag{16}
\end{aligned}$$

We note that comparing metric tensors requires a transformation that involves the pushforward (*i.e.*, transporting) of tangent spaces between the surfaces. This, in turn, necessitates the introduction of additional structure into our framework and thereby increases complexity. To minimize this complexity and make the comparison more tractable, we relax the notion of local distance—originally encoded by the metric tensor—to a more global measure on the surface by using pairwise geodesic distances. Incorporating this into our formulation, the distance becomes

$$D_{\text{soft}}(S_\alpha, S_\beta) = D_{\text{field}}^{\text{soft}}(S_\alpha, S_\beta) + D_{\text{geom}}^{\text{soft}}(S_\alpha, S_\beta), \tag{17}$$

where

$$\begin{aligned}
D_{\text{field}}^{\text{soft}}(S_\alpha, S_\beta) := & \sum_m \zeta_m \left(\frac{1}{2} \int_{S_\alpha} \int_{S_\beta} |f_\alpha^m(x) - f_\beta^m(y)|^p \right. \\
& \left. p(x, y) d\mu^\alpha(x) d\mu^\beta(y) + (S_\alpha \leftrightarrow S_\beta) \right)^{\frac{1}{p}},
\end{aligned}$$

$$\begin{aligned}
D_{\text{geom}}^{\text{soft}}(S_\alpha, S_\beta) = & \eta \left(\int_{S_\alpha^2} \int_{S_\beta^2} \frac{1}{2} |d_\alpha(x, x') - d_\beta(y, y')|^q p(x, y) \right. \\
& \left. p(x', y') d\mu^\alpha(x) d\mu^\alpha(x') d\mu^\beta(y) d\mu^\beta(y') + (S_\alpha \leftrightarrow S_\beta) \right)^{\frac{1}{q}}.
\end{aligned}$$

where $d_\alpha(x, x')$ and $d_\beta(y, y')$ denote the pairwise geodesic distances on S_α and S_β , respectively. Note that, since we are comparing pairs of points, we include an additional soft correspondence term $p(x', y')$ in the integral. Further, Eq. 17 is symmetric under exchange $S_\alpha \leftrightarrow S_\beta$. As we are going to use the meshes, we add a term which further strengthens the global structure

$$h_S(x, x') = \int_\Omega k_S(x, z) k_S(z, x') dz, \tag{18}$$

$$k_S(z, x') = \exp \left[-\frac{1}{2} \left(\frac{d_S(z, x')}{\sigma_S} \right)^2 \right], \tag{19}$$

then we define

$$G_S(x, x') = d_S(x, x') + \varepsilon_g h_S(x, x'), \tag{20}$$

where $d_S(x, x')$ denotes the pairwise geodesic distance on the surface S , and ε_g and σ_S are parameters controlling the contribution of global structure. So our final structural/geometric term is defined as

$$\begin{aligned}
D_{\text{Structure}}^{\text{soft}}(S_\alpha, S_\beta) = & \eta \left(\int_{S_\alpha^2} \int_{S_\beta^2} \frac{1}{2} \|G_\alpha(x, x') - G_\beta(y, y')\|^q p(x, y) \right. \\
& \left. p(x', y') d\mu^\alpha(x) d\mu^\alpha(x') d\mu^\beta(y) d\mu^\beta(y') + (S_\alpha \leftrightarrow S_\beta) \right)^{\frac{1}{q}}.
\end{aligned}$$

The IFACE Distance. We now define our distance, referred to as the **IFACE distance**, using the soft-correspondence values, based on the top- k normalized weights and their associated vertices. For each point, we select the k ($= 2$) largest values from the joint correspondence density weighted by local geometric measures:

$$\begin{aligned}
\tilde{w}^{y_k}(x) & \equiv \text{Normalize} \left(\text{Top}_k^y \left[p(x, y) \cdot \sqrt{|g_\alpha(x)| \cdot |g_\beta(y)|} \right] \right), \\
\tilde{w}^{x_k}(y) & \equiv \text{Normalize} \left(\text{Top}_k^x \left[p(x, y) \cdot \sqrt{|g_\alpha(x)| \cdot |g_\beta(y)|} \right] \right). \tag{21}
\end{aligned}$$

Here, $p(x, y)$ denotes the soft correspondence *density* between points $x \in S_\alpha$ and $y \in S_\beta$, and $|g_\alpha(x)|, |g_\beta(y)|$ are the determinants of the metric tensors at x and y , respectively. The Top operator selects the k largest weighted densities for each fixed variable (either x or y), and the Normalize operation ensures that the resulting weights form a valid probability distribution, *i.e.*, they integrate to 1 over the selected k -neighborhood.

Now, $\tilde{w}^{y_k}(x)$ represents a normalized soft distribution over the top- k points (y_k) on S_β that most strongly correspond to a given point $x \in S_\alpha$, and vice versa for $\tilde{w}^{x_k}(y)$.

Then the IFACE distance is defined as soft distance defined by the new weights as

$$D_{\text{IFACE}}(S_\alpha, S_\beta, k) = D_{\text{field}}(S_\alpha, S_\beta) + D_{\text{structure}}(S_\alpha, S_\beta), \tag{22}$$

where

$$\begin{aligned}
D_{\text{field}}(S_\alpha, S_\beta) = & \frac{1}{2^{1/p}} \sum_m \zeta_m \left(\sum_k \int_{S_\alpha} |f_\alpha^m(x) - f_\beta^m(y_k)|^p \tilde{w}^{y_k}(x) d^2x \right. \\
& \left. + \int_{S_\beta} |f_\alpha^m(x_k) - f_\beta^m(y)|^p \tilde{w}^{x_k}(y) d^2y \right)^{\frac{1}{p}}
\end{aligned}$$

$$\begin{aligned}
D_{\text{structure}}(S_\alpha, S_\beta) = & \frac{\eta}{2^{1/q}} \sum_{k, k'} \left(\int_{S_\alpha^2} \|G_\alpha(x, x') - G_\beta(y_k, y_{k'})\|^q \right. \\
& \tilde{w}^{y_k}(x) \tilde{w}^{y_{k'}}(x') d^2x d^2x' + \\
& \left. \int_{S_\beta^2} \|G_\alpha(x_k, x_{k'}) - G_\beta(y, y')\|^q \tilde{w}^{x_k}(y) \tilde{w}^{x_{k'}}(y') d^2y d^2y' \right)^{\frac{1}{q}}.
\end{aligned}$$

DISCRETE PROTEIN SURFACE

We use the discrete form of the problem as described in the main text. Here, we describe the protein surface generation pipeline, calculation of the marginal distribution used in the method, and the optimization process.

Protein Surface Generation. We use a modified MaSIF pipeline (github.com/jomimc/masif_molecule) to generate protein surfaces comprising vertex positions, connectivity information, and feature files describing vertex-level attributes, including charge, hydrophobicity (Kyte–Doolittle), Gaussian curvature, mean curvature, amino acid identity, and the sequence index of the corresponding residue. The resulting protein meshes are preprocessed for analysis and contain a maximum of 3,000 vertices per mesh.

Because optimization becomes computationally expensive for large mesh sizes, we simplify protein surface meshes while consistently transferring per-vertex geometric and chemical properties to the reduced representation. Starting from an input surface mesh, we first perform a cleaning step to remove invalid elements and disconnected components, producing a watertight mesh. The cleaned mesh is then decimated using quadric edge collapse to obtain a target resolution, with the number of faces proportional to the desired vertex count. After decimation, small isolated components are removed, and the mesh is further refined using Laplacian smoothing to reduce discretization noise while preserving overall surface geometry.

To propagate vertex-wise properties from the original mesh to the simplified mesh, we establish a correspondence based on spatial proximity. Specifically, each vertex of the simplified mesh is mapped to its nearest vertex on the original mesh using a KD-tree search. For each mapped vertex, we define a local neighborhood on the original mesh using a fixed number of hops in the vertex adjacency graph. Continuous-valued properties are transferred by averaging over these neighborhoods, whereas discrete or categorical properties are directly inherited from the corresponding nearest vertices.

Finally, we compute geometric descriptors, including mean and Gaussian curvature, directly on the simplified mesh. The resulting meshes and associated properties are saved for downstream analysis, ensuring a consistent and computationally efficient surface representation with a bounded number of vertices.

Calculation for marginal distributions. In this section, we provide the procedure used to calculate marginal distribution for the protein surfaces. Let $\{\mu_i^\alpha\}$ and $\{\mu_j^\beta\}$ denote the vertex areas of surfaces S_α and S_β , respectively. Let $f_i^{\alpha m}$ and $f_j^{\beta m}$ denote the feature fields, where $m \in$ (Electrostatic Potential, Hydrophobicity, Hydrogen Bond Propensity, Mean curvature). We compute the marginal distributions ρ_i^α and ρ_j^β as follows.

Step 1: Area-based density (constant field).

$$\rho_i^{\alpha(0)} = \frac{\mu_i^\alpha}{\sum_i \mu_i^\alpha}, \quad \rho_j^{\beta(0)} = \frac{\mu_j^\beta}{\sum_j \mu_j^\beta}. \quad (23)$$

Step 2: Global minimum feature value.

$$f_{\min}^{(m)} = \min \left(\min_i f_i^{\alpha(m)}, \min_j f_j^{\beta(m)} \right). \quad (24)$$

Step 3: Area-weighted, shifted features.

$$\tilde{f}_i^{\alpha(m)} = (f_i^{\alpha(m)} - f_{\min}^{(m)}) \mu_i^\alpha, \quad \tilde{f}_j^{\beta(m)} = (f_j^{\beta(m)} - f_{\min}^{(m)}) \mu_j^\beta. \quad (25)$$

Algorithm 1: Protein Mesh Alignment and Coupling Matrix Estimation

Input: Surface meshes S_α and S_β with vertex sets

$$\{x_i\}, \{y_j\}, \text{ associated vertex areas } \{\mu_i^\alpha\}, \{\mu_j^\beta\},$$

and m -feature fields $f_i^{\alpha(m)}, f_j^{\beta(m)}$.

Output: Optimal coupling matrix P_{ij} .

1. Initialize P_{ij} via rigid alignment followed by feature-aware nonrigid alignment.
2. Transform vertices and features:
 $x_i \rightarrow \tilde{x}_i, f_i^{\alpha(m)} \rightarrow \tilde{f}_i^{\alpha(m)}$.
3. Construct descriptor vectors
 $\tilde{X}_i = [\tilde{x}_i, \tilde{f}_i^{\alpha(m)}], Y_j = [y_j, f_j^{\beta(m)}]$.
4. Compute Gaussian affinity kernel $A_{ij} = \exp(-\|\tilde{X}_i - Y_j\|^2 / \delta^2)$ with $\delta = 0.01$.
5. Apply Sinkhorn normalization to the Gaussian affinity matrix.
6. Obtain initial coupling P_{ij} .
7. Optimize Eq. (30) with $\lambda = 0.9$.
8. Update P_{ij} .
9. Re-optimize Eq. (30) without entropic regularization.
10. Derive final coupling matrix P_{ij} .
11. Return P_{ij} .

Step 4: Feature normalization.

$$\tilde{f}_i^{\alpha(m)} \leftarrow \frac{\tilde{f}_i^{\alpha(m)}}{\sum_i \tilde{f}_i^{\alpha(m)}}, \quad \tilde{f}_j^{\beta(m)} \leftarrow \frac{\tilde{f}_j^{\beta(m)}}{\sum_j \tilde{f}_j^{\beta(m)}}. \quad (26)$$

Step 5: Combine area and feature distributions.

$$\rho_i^\alpha = \rho_i^{\alpha(0)} + \sum_m \tilde{f}_i^{\alpha(m)}, \quad \rho_j^\beta = \rho_j^{\beta(0)} + \sum_m \tilde{f}_j^{\beta(m)}. \quad (27)$$

Step 6: Final normalization.

$$\rho_i^\alpha \leftarrow \frac{\rho_i^\alpha}{\sum_i \rho_i^\alpha}, \quad \rho_j^\beta \leftarrow \frac{\rho_j^\beta}{\sum_j \rho_j^\beta}. \quad (28)$$

Optimization for finding optimal coupling matrix.

Optimization.— We perform a four-step refinement to obtain the coupling matrix P_{ij} , which includes mesh alignment followed by optimization steps. We first perform rigid alignment of the meshes using RANSAC⁴⁹ for coarse initialization, followed by Iterative Closest Point (ICP)^{50,51} for refinement. After that, we use non-rigid alignment in the combined real and feature space, employing the coherent point drift algorithm⁵². We convert the point sets into a Gaussian kernel to obtain a similarity measure between the transformed and target points. Then, we convert the Gaussian kernel into a coupling/soft-correspondence matrix using the Sinkhorn update^{47,48} with the marginal distribution. We feed that solution into the entropically regularized objective function for the field and structural terms with $\lambda = 0.9$. After that, we refine the coupling matrix by solving the objective function without entropic regularization. The algorithmic steps are given in Algorithm 1.

Non-rigid alignment for initializing coupling matrix.— After rigid alignment of meshes, we perform non-rigid registration in the joint geometric and feature space using the Coherent Point Drift (CPD) algorithm⁵². CPD models the source points as centroids of a Gaussian mixture and seeks a smooth non-rigid transformation that maximizes the likelihood of the target points under this model while enforcing motion coherence. Let $X \equiv [x_i, f_i^{\alpha(m)}]$ and $Y \equiv [y_j, f_j^{\beta(m)}]$ denote the source and target vertex sets, respectively, after rigid alignment in coordinate space, together with the m -feature-field values defined on those vertices. The non-rigid CPD transformation $T(\cdot)$ produces transformed points for source $\tilde{X} = \{T(X_i)\}$.

To quantify the similarity between transformed and target points, we construct a Gaussian kernel

$$A_{ij} = \exp\left(-\frac{\|\tilde{X}_i - Y_j\|^2}{\delta^2}\right), \quad (29)$$

which encodes pairwise affinities between \tilde{X} and Y . We then interpret A as an entropic-regularized similarity matrix and convert it into a soft correspondence (coupling) matrix by applying Sinkhorn iterations^{47,48} to match prescribed marginal distributions. This yields a doubly stochastic matrix P_{ij} , which serves as the initial coupling (soft correspondence) matrix. We set $\delta = 0.01$ to enforce a tight similarity constraint.

Entropic and entropic free regularized optimization of objective function.— We use the initial coupling matrix P_{ij} obtained using the above procedure as an initialization for the entropic optimization of the objective function combining the structural and field terms:

$$\begin{aligned} P_{ij}^{\text{entropic}} = \arg \min_{P_{ij}} & \left[(1 - \lambda) \mathcal{F}(S_\alpha, S_\beta) + \lambda \mathcal{S}(S_\alpha, S_\beta) \right. \\ & \left. - \varepsilon P_{ij} \log P_{ij} \right], \\ \text{subject to } & \sum_j P_{ij} = \rho_i^\alpha, \quad \sum_i P_{ij} = \rho_j^\beta, \end{aligned} \quad (30)$$

where $\mathcal{F}(S_\alpha, S_\beta)$ and $\mathcal{S}(S_\alpha, S_\beta)$ are the field and structural terms defined in the Methods section of the main text for the optimization. We use unit-normalized meshes to compute the distance matrices used in the structural term.

Weight parameters.— The parameter λ controls the balance between geometric correspondence and field alignment in the surface coupling matrix. We set $\lambda = 0.9$, giving dominant weight to the structural term so that the surface map remains geometrically continuous. The field term then acts as a secondary constraint that aligns regions with similar

physicochemical fields. While this contribution can break geometric symmetries, the strong structural weighting preserves the global organization of the correspondence.

To verify that this choice achieves the intended balance, we examined a controlled toy system consisting of ellipsoidal surfaces. The surfaces were geometrically identical but carried different charge distributions, allowing the influence of the field term to be isolated from geometry. Across the explored range of λ , smaller values emphasize agreement of the field term, whereas larger values emphasize geometric consistency. We observe qualitatively stable behavior for $\lambda \gtrsim 0.85$ and therefore select $\lambda = 0.9$, which maintains structural continuity while allowing the field contribution to guide feature-consistent alignment across the surface.

Entropic regularization parameter.— The entropic regularization parameter ε is chosen adaptively to maintain numerical stability during optimization. Specifically,

$$\varepsilon = \max\left(\frac{\max \mathcal{C}}{\kappa}, \tau \cdot \text{median}(\mathcal{C}), 10^{-6}\right), \quad (31)$$

where \mathcal{C} denotes the collection of cost matrices used in the optimization, including the structural matrices G_α, G_β and the field matrix $\mathcal{F}(S_\alpha, S_\beta)$. The maximum and median are taken over all scalar entries of these matrices. The constant κ prevents numerical underflow, while τ sets the regularization scale relative to the typical magnitude of the cost terms; we use $\kappa = 700$ and $\tau = 0.05$.

The entropically regularized problem is first solved to obtain an initial coupling P_{ij}^{entropic} . This solution is then used to initialize a second optimization without entropic regularization ($\varepsilon = 0$), yielding the final optimal coupling matrix P_{ij} . All optimizations were performed using the POT Python library^{53,54}. Across the dataset of 846 protein pairs, the full pipeline—including optimization and distance computations—takes about 8.5 minutes per pair on average. Experiments were conducted on a workstation equipped with an Intel Core i9-14900K CPU (24 cores, 32 threads) and 64 GB RAM running Ubuntu 24.04.3 LTS.

Color transfer between the mapped surfaces. Colors on the target surface c_j^{target} were computed by aggregating probability-weighted colors from matched vertices on the source surface c_i^{source} (e.g., target: 6XDS and source: 6XRX in Fig. 2), followed by normalization by the total incoming probability mass of the coupling matrix:

$$c_j^{\text{target}} = \frac{\sum_i P_{i \rightarrow j} c_i^{\text{source}}}{\sum_i P_{i \rightarrow j}}.$$

Here, the summation is restricted to the top two matches per i .